EES Catalysis

PAPER

View Article Online
View Journal | View Issue

Cite this: *EES Catal.*, 2025, 3, 1345

Optimization of competitive adsorption *via* oxygen vacancies on NiCo hydroxides for selective electrosynthesis of adipic acid coupled with hydrogen production†

Xun Pan, Lingzhi Sun, Kuang Chen, Jingui Zheng, Shaohan Xu, Chao Miao and Guohua Zhao *

The electrosynthesis of adipic acid through the cyclohexanol oxidation reaction (COR) can address the pollution issues associated with the traditional process. However, the complexity of the electrooxidation process and unclear dehydrogenation and oxidation mechanisms limit its application. Herein, we report oxygen vacancy (V_O) modification on NiCo hydroxides for the selective electrosynthesis of adipic acid. *In situ* IR and DFT calculations revealed significantly enhanced adsorption capacity and an optimized process for the co-adsorption of OH^- and organic compounds. The V_O promotes the conversion of ketone intermediates into glycol with the addition of H_2O while inhibiting the formation of ketone alcohols. *In situ* synchrotron radiation and Raman analyses reveal the reversible remodeling processes of Ni^{2+}–OH and Ni^{3+}–OOH during the COR. Consequently, V_O-NiCo demonstrated excellent COR performance (1.32 V *vs.* RHE onset potential) with conversion, adipic acid selectivity, and faradaic efficiency values of 98.4%, 95.6%, and 95.2%, respectively. The system generates 8.2 times more hydrogen compared with pure water splitting at the cathode. This integrated electrocatalytic system shows potential for large-scale production of H_2 and adipic acid, offering new insights for designing advanced electrocatalysts for cost-effective and sustainable energy conversion.

Received 6th May 2025,
Accepted 16th July 2025

DOI: 10.1039/d5ey00137d

rsc.li/eescatalysis

Broader context

The electrosynthesis of adipic acid *via* the cyclohexanol oxidation reaction (COR) is a green and sustainable method for upgrading biomass resources, which can address the pollution issues associated with traditional processes. However, the COR involves an eight-electron transfer process, and the dehydrogenation and oxidation mechanisms are not well understood, limiting its further application. In this study, we utilized oxygen vacancies to modulate the adsorption properties of cyclohexanol and OH^- on NiCo hydroxides to improve the conversion and selectivity for adipic acid. Oxygen vacancies promoted the addition reaction between the ketone intermediate and water to form geminal diols while inhibiting the formation of the ketol intermediate. This is crucial for steering the reaction towards the desired product. *In situ* synchrotron radiation and Raman spectroscopic analysis reveal the reversible remodeling processes of Ni^{2+}–OH and Ni^{3+}–OOH during the COR. Consequently, V_O-NiCo demonstrated excellent COR performance (1.32 V *vs.* RHE onset potential) with conversion, adipic acid selectivity, and faradaic efficiency values of 98.4%, 95.6%, and 95.2%, respectively. Moreover, this integrated electrocatalytic system generates 8.2 times more hydrogen compared with pure water splitting, offering new insights for cost-effective and sustainable energy conversion.

Introduction

Globally, the continuous consumption of fossil fuels and the resulting environmental pollution have increased the focus on renewable energy.[1–6] Biomass resources, owing to their abundance and renewability, have become a crucial pillar for sustainable development in the chemical industry. Through biomass conversion technologies, biomass can be efficiently transformed into various high-value chemicals and fuels, thereby reducing reliance on traditional fossil resources and mitigating environmental burdens.[4] Cyclohexanol (CHA) plays a significant role in green chemistry and sustainable development and is a widely utilized chemical raw material that can produce a variety of high-value organic intermediates.[7–9]

School of Chemical Science and Engineering, Key Laboratory of Spine and Spinal Cord Injury Repair and Regeneration Tongji Hospital, Tongji University 1239 Siping Road, Shanghai 200092, P. R. China. E-mail: g.zhao@tongji.edu.cn

† Electronic supplementary information (ESI) available. See DOI: https://doi.org/10.1039/d5ey00137d

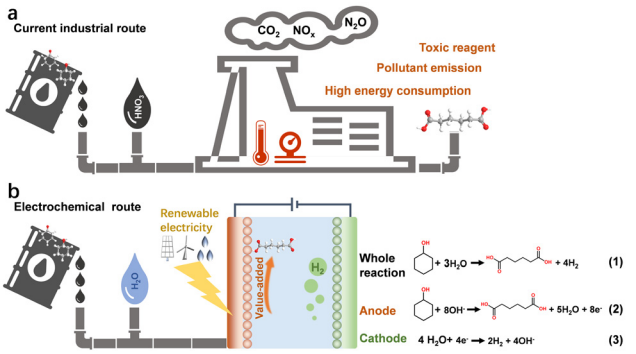

Scheme 1 (a) Illustration of the current industrial route. (b) Electrochemical route for the synthesis of AA from CHA.

Among these, adipic acid (AA) stands out as a highly valuable downstream product of CHA, serving as an essential raw material for various polymers, pharmaceuticals, lubricants, plasticizers, and food additives, with significant global market demand anticipated in the future.[10–12]

The conventional industrial method involves reacting a mixture of CHA and cyclohexanone (CHN) with nitric acid to produce AA. The procedure requires the use of a significant quantity of catalysts (such as Mo, W, and Cu) and various chemicals, leading to the production of considerable amounts of pollutants, including nitrogen oxides, nitrates, and heavy metals. This necessitates the implementation of efficient waste treatment systems to manage these hazardous materials. Consequently, this not only increases environmental strain but also results in increased treatment costs and presents technical challenges (Scheme 1a).[13–15] Electrochemical CHA oxidation (COR) provides an alternative method for producing AA under ambient conditions, and it can replace the slow oxygen evolution reaction (OER) at the anode, leading to more efficient hydrogen generation at low cell potentials (Scheme 1b).[16–19] The process is powered by renewable energy with no additional pollution. Unlike the OER, the COR encompasses the adsorption and conversion processes of CHA and OH^-. Many reports indicate that OH^- adsorbed on the catalyst surface gradually transforms into *OH or *OOH intermediates, which are crucial active species for the dehydrogenation and oxidation of various alcohols.[20–23] Hence, managing the competition between CHA and OH^- adsorption on the catalyst surface is essential for the efficient production of AA. Moreover, the COR process includes the ring cleavage of CHN, frequently yielding by-products such as glutaric acid (GA) and succinic acid (SA).[24,25] The primary challenge is to adjust the electronic structure of the catalyst and develop a rational catalyst to enhance the selectivity of AA.

Transition metal hydroxyl oxides (NiOOH, CoOOH and CuOOH *etc.*) can exhibit stunning performance in organic-electrolytic oxidation reactions in alkaline solution, such as the electrooxidation of 5-hydroxymethylfurfural (HMFOR),[26–31] benzyl alcohol (BOR),[32–34] and amine (AOR)[35–39] and there have been a few reports of this process in COR.[16,18,25,40] When voltages surpass approximately 1.35 V *vs.* RHE, NiOOH species, which function as the true active phase in Ni-based catalysts, typically exhibit a high reaction energy barrier.[32,41] Conversely, Co-based catalysts often show the capability of oxidizing at significantly lower onset potentials.[42–44] Thus, the combination of Ni and Co sites is expected to produce a synergistic effect in the electrocatalytic oxidation of COR, leading to reduced onset potentials and increased oxidation current densities. Furthermore, the catalytic performance of the active site can be enhanced by modifying the ligand structure of the catalyst and optimizing the competitive adsorption of organic molecules and OH^- in alkaline environments. Oxygen vacancies (V_O) defects offer a promising strategy to modify the surface electronic structure and the intrinsic electrocatalytic activity.[41,44–46] Previous research has indicated that V_O can optimize the surface adsorption energy and coupling of biomass substrates and OH^- on the electrocatalyst surface.[47] This optimization is crucial for enhancing the CHA dehydrooxidation and ring cleavage processes, thereby facilitating the efficient and highly selective production of AA.[48]

In this study, we introduce a NiCo hydroxide catalyst featuring oxygen vacancy defects (V_O-NiCo(OH)$_2$) for the conversion of CHA into AA. Density functional theory (DFT) computations reveal that V_O significantly improve the adsorption capabilities for both hydroxide (OH^-) species and organic molecules. The combination of *in situ* Raman spectroscopy and synchrotron radiation techniques has confirmed that the presence of V_O promotes the electrochemical transformation of NiCo(OH)$_2$ into NiCoOOH, thereby expediting the dehydrogenation of CHA. Further DFT and *in situ* infrared (IR) studies indicate that the V_O favors the preferential conversion of the CHN intermediate into glycol over ketol on the catalyst surface, leading to an enhanced selectivity for AA at 95.6%. This research underscores the efficacy of vacancy-engineered electrochemical pathways for the conversion of CHA into AA, highlighting a promising approach for the valorization of biomass into high-value chemicals.

Results and discussion

Preparation and characterization of electrocatalyst

Initially, we synthesized NiCo ultrathin metal–organic frameworks (NiCo-UMOFNs) derived from terephthalic acid through a straightforward ultrasonic fabrication technique. As illustrated in Scheme S1 (ESI†), oxygen vacancy-enriched V_O-NiCo(OH)$_2$ was synthesized through a $NaNH_2$ chemical reduction method. For comparative analysis, a vacancy-deficient NiCo(OH)$_2$ was produced *via* a similar technique, utilizing NiCo-UMOFNs that had been immersed in a strong alkali solution (3 M KOH). The powder X-ray diffraction (XRD) pattern of the as-prepared samples V_O-NiCo(OH)$_2$ and NiCo(OH)$_2$ (Fig. S1, ESI†) indicated that the Ni–Co precursor was composed of the mixed phases of Ni(OH)$_2$ (JCPDS no. 38-0715) and Co(OH)$_2$ (JCPDS no. 02-0925).[49] Scanning electron microscopy (SEM) images revealed that V_O-NiCo(OH)$_2$ consists of nanoflakes with a thickness of 10–20 nm, which can improve electrical conductivity and expose more active sites, contributing to enhanced electrocatalytic performance (Fig. S2a, ESI†). Transmission electron microscopy (TEM) also verified the ultrathin structure of V_O-NiCo(OH)$_2$ (Fig. S2b–d, ESI†).

High-resolution TEM (HR-TEM) images revealed a lattice spacing of 0.452 nm for V_O-NiCo(OH)$_2$. Energy-dispersive spectroscopy (EDS) elemental mapping confirmed the homogeneous distribution of Ni, Co, and O elements across the V_O-NiCo(OH)$_2$ nanosheets (Fig. 2e–h).

To precisely elucidate the defects present in the synthesized nanosheets, an initial investigation was conducted using X-ray photoelectron spectroscopy (XPS) analysis. As depicted in Fig. 1a, the Ni 2p core level spectra for both V_O-NiCo(OH)$_2$ and NiCo(OH)$_2$ reveal a pair of spin–orbit doublets, namely Ni $2p_{3/2}$ and Ni $2p_{1/2}$, which are indicative of the Ni^{2+} ion, along with their respective shakeup satellite features. Notably, the distinctive absorption peaks of V_O-NiCo(OH)$_2$ exhibit a shift towards lower energy levels in comparison to the benchmark NiCo(OH)$_2$, indicating that the presence of oxygen vacancies contributes to a reduction in the oxidation state of nickel. A similar trend is also evident in the Co spectrum (Fig. 1b). Analysis of the O 1s spectrum (Fig. S3, ESI†) reveals three distinct peaks at 530.86, 531.85, and 533.11 eV, corresponding to metal–hydroxide interactions, oxygen atoms adjacent to oxygen vacancies, and water molecules adsorbed on the surface, respectively. In comparison to the O 1s spectra of NiCo(OH)$_2$, it is clear that V_O-NiCo(OH)$_2$ exhibits a higher concentration of oxygen vacancies. Electron paramagnetic resonance (EPR) spectroscopy (Fig. S4, ESI†) was conducted at ambient temperature to investigate the chemical milieu surrounding the unpaired electrons. A pronounced EPR signal was detected at g = 2.002, suggesting that the electrochemically modified material exhibits an increased density of unpaired electrons and the presence of oxygen vacancy defects. To investigate the atomic architecture in greater detail, X-ray absorption fine structure spectroscopy (XAFS) was utilized. As illustrated in Fig. 2c, the Ni K-edge X-ray absorption near-edge structure (XANES) spectra indicate that the reduction by $NaNH_2$

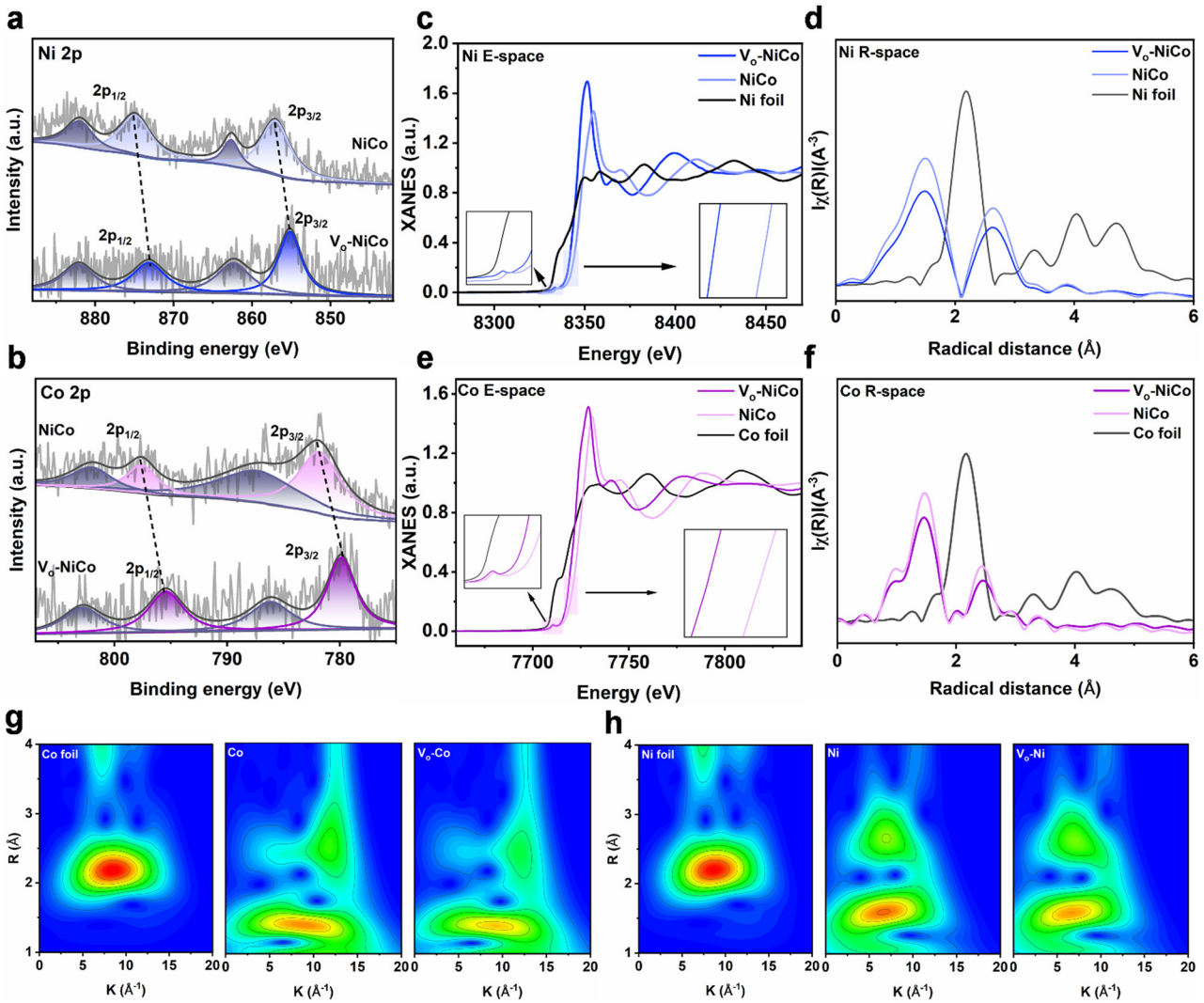

Fig. 1 (a) Ni and (b) Co 2p XPS spectra for V_O-NiCo and NiCo. X-ray absorption spectra (XAS) of the V_O-NiCo and NiCo. X-ray absorption near-edge structure (XANES) spectra of (c) the Ni K-edge and (e) Co K-edge. Edge X-ray absorption fine structure (EXAFS) spectra of (d) the Ni K-edge and (f) Co K-edge. WT contour of (g) the Ni K-edge and (h) Co K-edge.

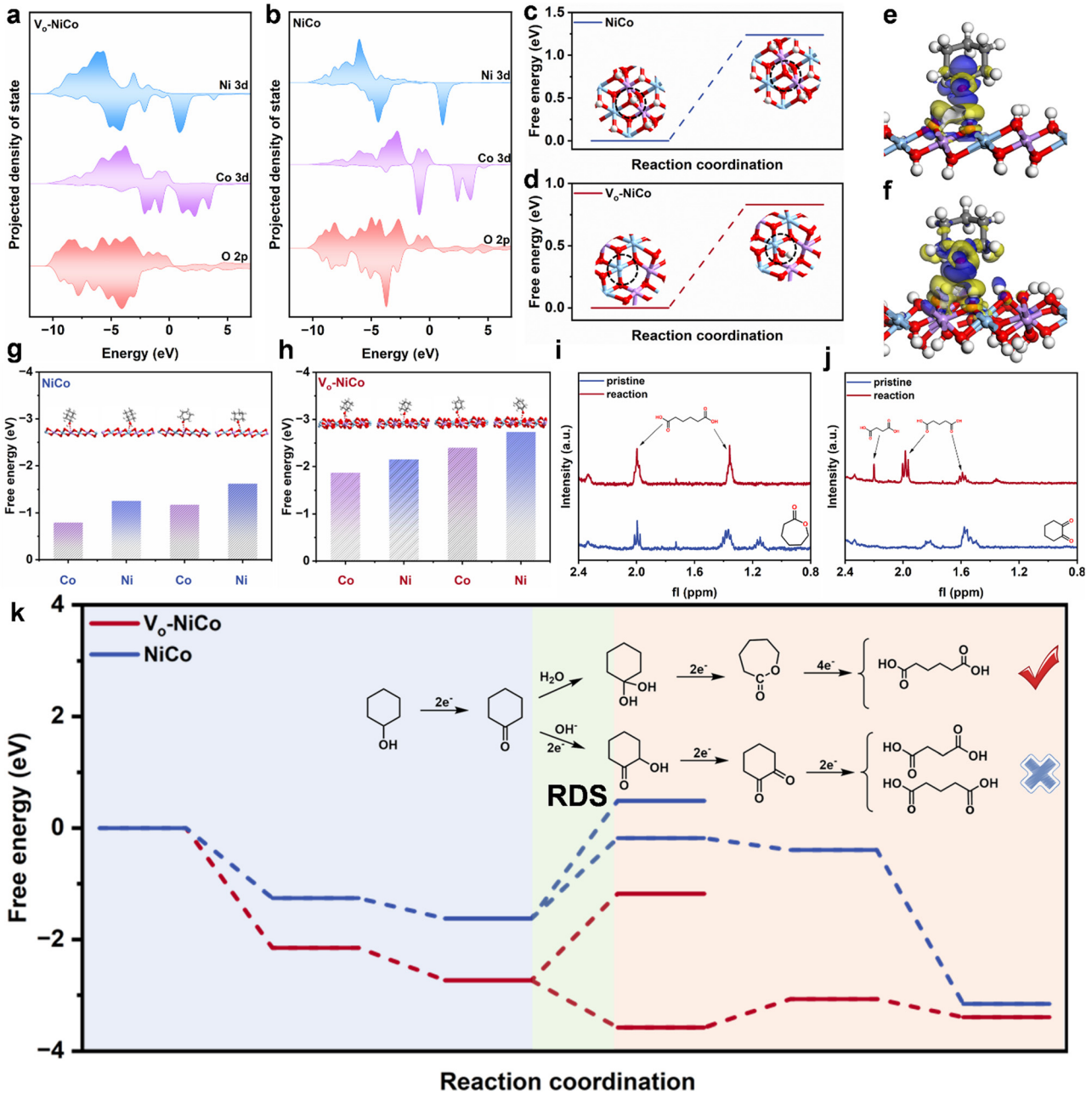

Fig. 2 PDOS of (a) V_O-NiCo(OH)$_2$ and (b) NiCo(OH)$_2$. (c) The dehydrogenation energy of *H on NiCo(OH)$_2$. (d) The adsorption energy of *OH on V_O-NiCo(OH)$_2$. Charge density differences of CHN adsorbed on (e) NiCo(OH)$_2$ and (f) V_O-NiCo(OH)$_2$. Adsorption energy of CHA and CHN on the Ni and Co sites of (g) NiCo(OH)$_2$ and (h) V_O-NiCo(OH)$_2$. ^{1}H NMR spectra of the reaction using V_O-NiCo(OH)$_2$ electrodes, (i) ε-caprolactone and (j) cyclohexanedione. (k) Pathways of CHA oxidation on V_O-NiCo(OH)$_2$ and (b) NiCo(OH)$_2$.

causes a displacement of the Ni atom towards lower energy levels, implying that the average oxidation state of the Ni cation in V_O-NiCo(OH)$_2$ is notably diminished compared to that in NiCo(OH)$_2$. The presence of abundant oxygen vacancies in V_O-NiCo(OH)$_2$ results in a plethora of coordination-unsaturated Ni sites characterized by a reduced oxidation state.

The Ni K-edge Fourier-transformed extended X-ray absorption fine structure (FT EXAFS) spectra of V_O-NiCo(OH)$_2$ and NiCo(OH)$_2$ reveal two distinct peaks at approximately 1.6 Å and 2.7 Å, corresponding to the first Ni–O shell and the second Ni–Ni (Ni–O–Ni) shell contributions, respectively (Fig. 2d). The intensities of the Ni–O and Ni–Ni peaks in V_O-NiCo(OH)$_2$ are markedly diminished compared to those in NiCo(OH)$_2$, indicating that the average coordination numbers for Ni–O and Ni–Ni in V_O-NiCo(OH)$_2$ are significantly lower than in NiCo(OH)$_2$. Furthermore, the defect structure, characterized by reduced coordination numbers, contributes to a contraction of the Ni–O–Ni bond length in V_O-NiCo(OH)$_2$. In an ideal NiCo(OH)$_2$ devoid of oxygen vacancies, the theoretical coordination number for Ni–O is 5.87. The outcomes of EXAFS fitting the *R*-space for Ni and Co in

the two catalysts are presented in Fig. S5, S6 and Tables S1, S2 (ESI†). The analysis reveals coordination numbers of 4.71 for Ni–O in V_O-$NiCo(OH)_2$, respectively, thus confirming the presence of oxygen vacancies in this sample. The EXAFS analysis for Co demonstrated a similar pattern to that of Ni (Fig. 2e and f), indicating that oxygen vacancies lead to a reduction in the Co valence state and a concomitant decrease in the coordination number, with peaks identified at approximately 1.6 Å and 2.3 Å. Collectively, these observations suggest that the electrochemical treatment facilitates the formation of oxygen vacancies in $NiCo(OH)_2$, resulting in a slight decrease in metal valence states and the emergence of numerous unsaturated coordinated Ni and Co centers. This enhancement is critical for the subsequent formation of potential oxidatively active species, such as NiOOH and CoOOH. Additionally, the presence of oxygen vacancies may improve the adsorption affinity of active sites for organic molecules, influence intermediate reaction pathways, and enhance the selectivity for the conversion of target molecules, which is pivotal for the efficient transformation of CHA into AA.

Theoretical analysis of the role of oxygen vacancies

To elucidate the influence of oxygen vacancies on the intrinsic catalytic activity, we conducted density functional theory (DFT) simulations. As depicted in Fig. 2a and b, the d-band centers of V_O-$NiCo(OH)_2$ exhibited an upward shift relative to $NiCo(OH)_2$, signifying a modification in the local electronic environment due to the presence of oxygen vacancies, which enhances the interaction with adsorbates. Furthermore, the charge density at the Fermi level increased, resulting in a greater overlap between the Ni/Co d orbitals and the O p orbitals near the Fermi energy. This observation indicates an elevated degree of hybridization between the d orbitals of Ni/Co and the p orbitals of O, facilitating a more rapid charge transfer between Ni/Co and O. Consequently, oxygen vacancies have been demonstrated to augment the intrinsic activity of the catalysts.

Existing literature indicates that during electrooxidation, Ni and Co catalysts are typically transformed into high-valent oxidatively active species such as NiOOH or CoOOH.[26,43,50] In the case of NiCo bimetallic materials, NiOOH generally displays more pronounced oxidative activity, while Co primarily serves to modulate Ni's electronic structure and reduce the onset potential from Ni^{2+} to Ni^{3+}.[51–54] Therefore, our theoretical investigations into the formation of active species focus on the variations associated with Ni. The coordination-saturated $NiCo(OH)_2$ typically undergoes a preferential one-electron oxidation to yield the active species NiOOH during electrooxidation, subsequently participating in the oxidation of organic substrates (Fig. 2c). Thus, we initially calculated the free energy of the reaction for $NiCo(OH)_2$ undergoing one-electron oxidation, which was determined to be 1.20 eV. In parallel, we performed a similar theoretical assessment for V_O-$NiCo(OH)_2$, yielding a free energy of 1.18 eV (Fig. S7, ESI†). This indicates that the introduction of oxygen vacancies does not alter the one-electron dehydrogenation process of NiCo hydroxide to form NiOOH. Notably, V_O-$NiCo(OH)_2$, with its oxygen vacancies, can also transition to high-valent metal species *via* the adsorption of OH^-. Accordingly, we calculated the reaction free energy for the formation of NiOOH through this pathway, resulting in a value of 0.79 eV, which is significantly lower than that of the dehydrogenation pathway (Fig. 2d). Based on the aforementioned analysis, we propose that the introduction of oxygen vacancies modifies the generation pathway of the originally active species while enhancing the conversion efficiency of NiOOH.

The incorporation of oxygen vacancies modulates the adsorption behavior of OH^- and organic molecules at the active sites, significantly impacting the dehydrogenation of cyclohexanol (CHA) and the subsequent oxidation reactions. Given that the more precisely defined reactants in the synthetic pathway of acetic acid (AA) are CHA and cyclohexanone (CHN), we conducted a comparative analysis of the adsorption of these two organic compounds on the two catalysts individually. For the Ni site, as illustrated in Fig. 2g and h, the adsorption energies for CHA and CHN on $NiCo(OH)_2$ were measured at −1.25 eV and −1.62 eV, respectively, which are notably lower than the values of −2.15 eV and −2.73 eV observed on V_O-$NiCo(OH)_2$. This suggests that the presence of oxygen vacancies enhances the adsorption of hydroxyl and keto oxygens at the active sites, promoting subsequent oxidation processes. This observation aligns with our intended catalyst design principles. Furthermore, to elucidate the adsorption characteristics of the NiCo bimetallic materials, we also determined the adsorption energies for CHA and CHN on Co within V_O-$NiCo(OH)_2$. The findings indicate that the adsorption energies for Co are inferior to those for Ni concerning both CHA and CHN, likely attributable to the more pronounced vacancy interactions associated with Ni. An increased number of oxygen vacancies leads to a greater electron deficiency in the d orbitals of Ni, thereby enhancing the likelihood of hydroxyl and keto oxygen attack.

The reaction pathway of CHA on V_O-$NiCo(OH)_2$ and $NiCo(OH)_2$ is illustrated in Fig. 2k. The electrooxidation process of CHA to CHN involves a transfer of 8 electrons in total, with CHN identified as the most distinct intermediate arising from the initial 2-electron oxidation, according to existing literature.[19,40,55] In the blue section of Fig. 2k, it can be seen that the reaction energy barrier for CHA on V_O-$NiCo(OH)_2$ is −0.58 eV, which is greater than the −0.37 eV barrier for $NiCo(OH)_2$, suggesting that the presence of oxygen vacancies facilitates the electrooxidation of CHA. The following steps, involving the ring opening and oxidation of CHN, require further investigation, as the intermediates are not easily detectable. It has been noted that CHN can reversibly convert to the enol in alkaline environments, followed by a 2-electron oxidation to yield the intermediate 2-hydroxycyclohexanone. This is succeeded by another 2-electron oxidation, resulting in the critical intermediate cyclohexanedione. Ultimately, cyclohexanedione undergoes C–C bond cleavage and a 2-electron transfer to produce AA. An alternative pathway suggests that CHN may first engage in an addition-like reaction in alkaline conditions, where OH^- preferentially attacks the C_α position, forming the key intermediate 1,1-dihydroxycyclohexane, which is then

oxidized *via* a 2-electron process to yield ε-caprolactone. Finally, ε-caprolactone undergoes a 4-electron oxidation leading to the formation of AA. To elucidate the intermediates involved in the oxidation of CHN to AA and to assess the influence of oxygen vacancies on selectivity enhancement, we chose the crucial intermediates from both pathways, ε-caprolactone and cyclohexanedione, as substrates for electrooxidation and analyzed the product distribution using NMR. As depicted in Fig. 2i, ε-caprolactone undergoes complete conversion, yielding only AA with a selectivity nearing 100%. In contrast, the products derived from cyclohexanedione are exclusively glutaric acid and succinic acid (Fig. 2j). Consequently, we propose that the key to achieving high selectivity in the production of AA from CHA as a substrate lies in enhancing the attack of *OH on the C_α atoms to produce 1,1-dihydroxycyclohexane, which subsequently leads to the formation of ε-caprolactone. Thus, we conducted a differential charge density analysis on the adsorption models of CHN on the catalysts V_O-$NiCo(OH)_2$ and $NiCo(OH)_2$. A comparative examination of Fig. 2e-f reveals that the charge density associated with CHN is significantly greater on V_O-$NiCo(OH)_2$, suggesting its superior catalytic efficacy for CHN conversion. The electron deficiency is particularly pronounced at the C_α position, facilitating the nucleophilic attack of *OH on C_α, thereby yielding the targeted intermediate 1,1-dihydroxycyclohexane. Subsequently, we analyzed the reaction pathways for cyclohexanone on both V_O-$NiCo(OH)_2$ and $NiCo(OH)_2$ through theoretical computations. As illustrated in the green region of Fig. 2k, pure $NiCo(OH)_2$ shows minimal differentiation between the two reaction pathways. In contrast, the presence of oxygen vacancies substantially decreases the free energy barrier for the transformation from cyclohexanone to 1,1-dihydroxycyclohexane, reducing it from 1.44 eV to −0.84 eV. A plausible mechanistic insight is that the hydroxide ions (OH^-) adsorbed at the oxygen vacancies are more predisposed to attack the C_α atoms of CHN, thereby favoring the selectivity toward the formation of 1,1-dihydroxycyclohexane and suppressing the production of 2-hydroxycyclohexanone. The reaction pathways for cyclohexanone on V_O-$NiCo(OH)_2$ and $NiCo(OH)_2$ are presented in the inset of Fig. 2k. This discussion supports the conclusion that the incorporation of oxygen vacancies not only enhances the catalytic activity of the metal active sites but also optimizes the adsorption dynamics of reactants and hydroxide ions on the catalyst surface, effectively facilitating the delivery of active OH^- species and promoting the selective and efficient synthesis of AA.

Electrochemical cathodic COR performance

The electrocatalytic performance of V_O-$NiCo(OH)_2$ and $NiCo(OH)_2$ for cathodic and anodic reactions was assessed using a standard three-electrode configuration in a 1.0 M KOH electrolyte, with and without the addition of 20 mM CHA. Analysis of the linear sweep voltammetry (LSV) data presented in Fig. 3a reveals that the onset potential for V_O-$NiCo(OH)_2$ during COR was 1.32 V *vs.* RHE. It can achieve a current density of 10 mA cm^{-2} at 1.36 V *vs.* RHE, which is significantly lower than the 1.42 V *vs.* RHE required for $NiCo(OH)_2$. Moreover, in the absence of CHA, V_O-$NiCo(OH)_2$ demands a potential of 1.55 V *vs.* RHE to reach the same current density, suggesting a greater propensity for COR compared to OER. To elucidate the roles of Ni and Co in the COR progress on V_O-$NiCo(OH)_2$, we conducted LSV tests for V_O-$Ni(OH)_2$ and V_O-$Co(OH)_2$. As shown in Fig. S8a, b (ESI†), it is evident that both V_O-$Ni(OH)_2$ and V_O-$Co(OH)_2$ have a catalytic effect on COR, as indicated by the increase in current density upon the addition of CHA. In Fig. S8c, d (ESI†) the current densities of the three catalysts during the COR reaction are compared, showing that the V_O-$Co(OH)_2$ catalyst has the weakest capability for COR, while V_O-$Ni(OH)_2$ exhibits better catalytic performance. Moreover, with the introduction of the second metal Co, V_O-$NiCo(OH)_2$ demonstrates a lower onset potential and higher current density. Therefore, Ni is primarily responsible for the catalytic oxidation, while Co functions to modulate the electronic structure of Ni, facilitating the formation of the active oxidation species NiOOH at lower potentials, thereby enhancing the catalytic oxidation of CHA.

To verify the effect of V_O for balancing the competing adsorption of OH^- and CHA on the catalyst surface, we analyzed the formation rate of AA at different substrate concentrations (Fig. 3b). Chronoamperometry measurements were conducted to examine the electrochemical kinetic process from CHA to AA, and the potential was 1.46 V *vs.* RHE.[56,57] We first tested the dependency of the partial current density for AA at different OH^- concentrations (0.1–2 M) with 20 mM CHA. Both catalysts demonstrated a linear relationship between the rate of AA and OH^- concentration, whereas the V_O-$NiCo(OH)_2$ (0.60) showed a higher reaction order than $NiCo(OH)_2$ (0.48). Under a constant KOH concentration (1 M), the formation rate of AA on V_O-$NiCo(OH)_2$ also showed a linear relationship when the CHA concentration was below 200 mM. In contrast, for $NiCo(OH)_2$, the reaction order decreased from 0.48 to 0.05 after 100 mM. This indicates that the presence of oxygen vacancies can enhance the adsorption of CHA on the catalyst surface, thereby promoting the reaction kinetics of COR. Additionally, V_O-$NiCo(OH)_2$ demonstrates a significantly reduced Tafel slope of 53.5 mV dec^{-1}, in contrast to the 83.5 mV dec^{-1} observed for $NiCo(OH)_2$ (Fig. 3c), indicating a more rapid electron transfer kinetics for COR. The turnover frequency (TOF) analysis further indicates that the V_O-$NiCo(OH)_2$ catalyst possesses an elevated TOF, signifying enhanced intrinsic activity at its active sites. Furthermore, a comparative assessment of the electrochemical surface areas (ECSA) for both catalysts was performed. As shown in Fig. S9 (ESI†), the double-layer capacitance (C_{dl}) values for V_O-$NiCo(OH)_2$ were found to be 4.5 and 3.9 mF cm^{-2} during OER and COR, respectively, while the corresponding values for $NiCo(OH)_2$ were 4.0 and 3.4 mF cm^{-2}. These results demonstrate that the incorporation of oxygen vacancies improved the catalytic efficacy for $NiCo(OH)_2$ during COR (Fig. S10, ESI†). To gain a deeper insight into the high current density achieved by CHA at low potentials, intermittent electrochemical measurements were performed by applying potentials to V_O-$NiCo(OH)_2$ to investigate the COR adsorption behavior. Initially, a potential of 1.46 V *vs.* RHE was applied in 1 M KOH to activate the catalyst and

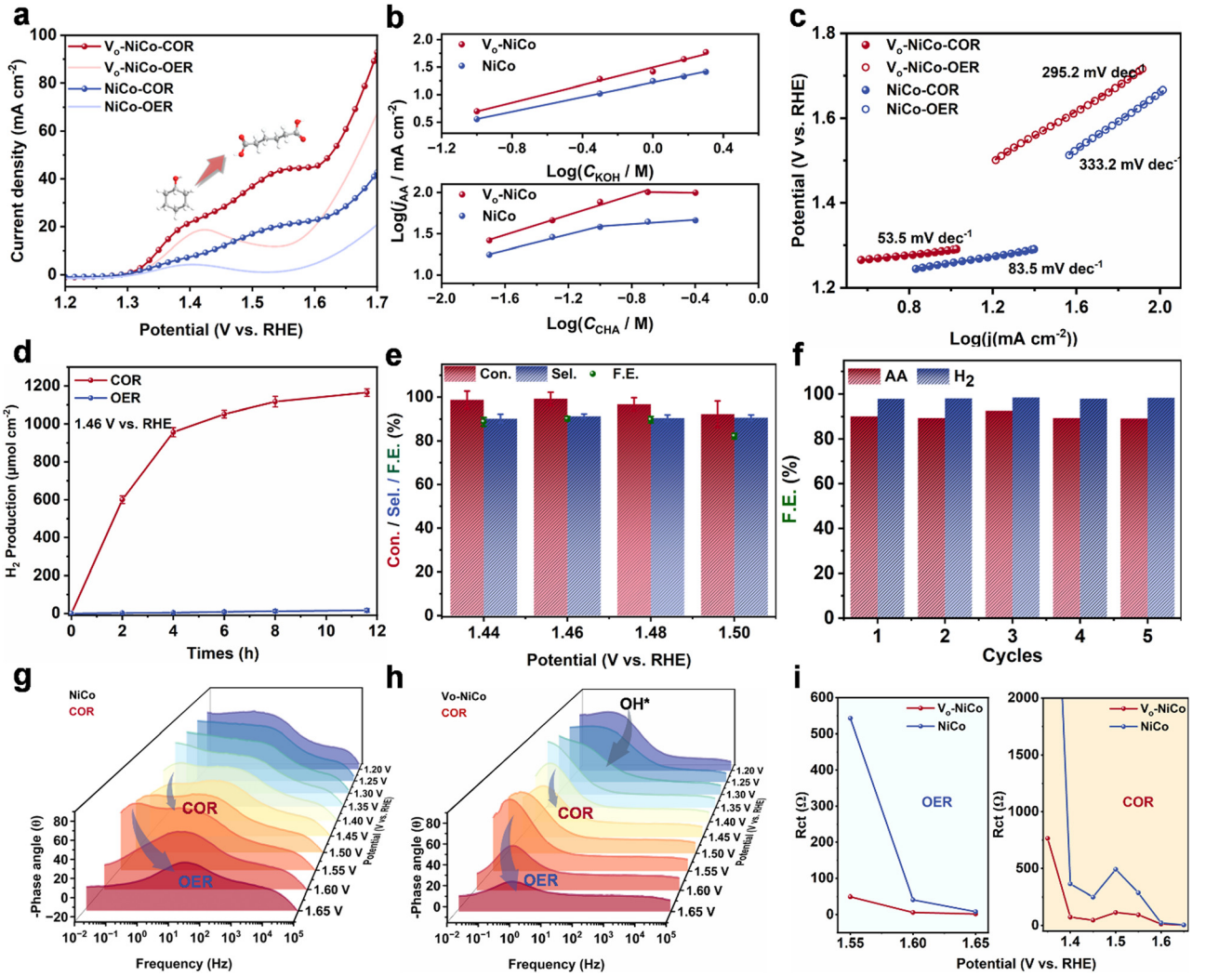

Fig. 3 (a) LSV curves of V_O-NiCo(OH)$_2$ and NiCo(OH)$_2$ in KOH solution with and without 20 mM CHA. (b) Partial current density of AA as a function of substrate concentration (OH^- and CHA) in a 20 mM CHA electrolyte over V_O-NiCo(OH)$_2$ and V_O-NiCo(OH)$_2$. (c) The Tafel data of the prepared V_O-NiCo(OH)$_2$ and NiCo(OH)$_2$ for the COR and OER. (d) H_2 production for the COR and OER in 1.46 V *vs.* RHE. (e) CHA conversion, AA selectivity and faradaic efficiency obtained for V_O-NiCo(OH)$_2$ at different potentials. (f) AA faradaic efficiency and H_2 production obtained for five cycles. Bode phase plots of the *in situ* electrochemical impedance spectra of (g) NiCo(OH)$_2$ and (h) V_O-NiCo(OH)$_2$ during the COR. (i) The resistance of the interfacial charge transfer reaction of NiCo(OH)$_2$ and V_O-NiCo(OH)$_2$ during the OER and COR.

facilitate the transition from low- to high-valent metal species. Subsequently, a potential of 1.00 V *vs.* RHE was applied after maintaining the open circuit potential for a period, resulting in a pronounced transient current. This transient current was significantly reduced when CHA was introduced midway or directly during COR (Fig. S11, ESI†). It indicates that CHA oxidation is associated with the formation of high-valent metal species at low potentials, which is crucial for achieving higher anodic current in COR compared to OER.

To further demonstrate the advantage of COR over OER for synergistic hydrogen production, we compared the hydrogen production performance at 1.46 V *vs.* RHE. As depicted in Fig. 3d, the total hydrogen production from the electrochemical oxidation of 20 mM CHA substrate at 1.46 V *vs.* RHE was 1185.6 μmol cm^{-2}, whereas the OER was 31.4 μmol cm^{-2}, indicating that COR enhances H_2 production at the cathode. The effectiveness of COR was evaluated by characterizing the product using NMR at different potentials. An H-type two-compartment cell was employed as the reaction setup, containing 15 mL of electrolyte with 20 mM CHA in the anodic compartment, and the total charge for complete reaction was 232 C. As shown in Fig. 3e and Fig. S12 (ESI†), CHA was almost entirely converted when the transferred charge reached 232 C. The optimal potential for the reaction was 1.46 V *vs.* RHE, yielding a 95.6% selectivity for AA and a 95.2% Faraday efficiency. However, all COR indicators significantly declined at 1.50 V *vs.* RHE due to the weak competitive OER. Additionally, similar tests with NiCo(OH)$_2$ electrodes at 1.46 V *vs.* RHE demonstrated a marked decrease in the conversion and selectivity of AA in systems lacking oxygen vacancies, suggesting their role in enhancing adipic acid selectivity (Fig. S13, ESI†). Fig. S14 (ESI†) represents the product test of V_O-NiCo(OH)$_2$, V_O-Ni(OH)$_2$ and V_O-Co(OH)$_2$ electrodes for the COR after 10 h with a

reaction potential of 1.46 V *vs.* RHE. The conversion rate of CHA on V_O-Ni$(OH)_2$ is relatively low, and the unreacted intermediate CHN is clearly observed. V_O-Co$(OH)_2$ shows even poorer catalytic performance for COR, with the initial reactant CHA still detectable in the electrolyte. This indicates that Ni serves as the primary active site during COR on the V_O-NiCo$(OH)_2$. Catalyst stability was assessed as shown in Fig. 3f, demonstrating that the Faraday efficiency of anodic adipic acid remained at 90% after five reaction cycles, while the cathodic hydrogen production efficiency remained close to 100%. We performed XPS characterization of the V_O-NiCo$(OH)_2$ after the COR. As shown in Fig. S15 (ESI†), the Ni 2 $p_{3/2}$ peak of V_O-NiCo$(OH)_2$ centered at 855.6 eV, which is almost identical to the value of 855.3 eV before the reaction. The Co 2 $p_{3/2}$ shows a new peak at 782.6 eV, which can be attributed to the Co^{3+}–OOH generated during the electrocatalytic process. As reported in the literature, both Ni and Co will be transformed into Ni^{3+}–OOH and Co^{3+}–OOH with an applied potential.[52–54] Since the main reactive species is Ni^{3+}–OOH, which can undergo a redox reaction with cyclohexanol, the valence state of Ni will decrease to Ni^{2+} after the COR, while Co can remain Co^{3+}. Meanwhile, O 1s exhibits a stronger peak at 531.67 eV, which corresponds to the OH^- adsorbed at the oxygen vacancies. This indicates that the oxygen vacancies remain stable after the reaction. To further demonstrate the stability of the oxygen vacancies during COR, EPR analysis was used to examine the catalyst after the COR. As shown in Fig. S16 (ESI†), the catalysts exhibited almost the same oxygen vacancy strength, indicating that the oxygen vacancies can be stabilized to function in COR.

Electrochemical impedance spectroscopy (EIS) was utilized to examine the electron transfer processes and reaction kinetics of NiCo$(OH)_2$ and V_O-NiCo$(OH)_2$. The high-frequency interface corresponds to the oxidation occurring within the electrode, whereas the low-frequency region is associated with charge distribution resulting from the generation of oxidizing species at the electrode surface. An inflection point indicating sluggish OER kinetics was detected in the low-frequency range (10^{-2}–10^{0} Hz) beyond 1.55 V *vs.* RHE (Fig. S17, ESI†), consistent with earlier findings.[28,58] For NiCo$(OH)_2$ during COR, the introduction of CHA shifted this inflection point to 1.40 V *vs.* RHE, with the COR signature appearing in the mid-frequency domain (10^{-1}–10 Hz) (Fig. 3g). In comparison to NiCo$(OH)_2$, the phase angle of the transition peaks related to COR on the surface of V_O-NiCo$(OH)_2$ is reduced at the same voltage. This indicated that the introduction of V_O can enhance the proton transfer process of CHA at the electrode interface. (Fig. 3h). As demonstrated in Fig. 3i, the introduction of V_O can significantly improve the conductivity of the catalyst. During the COR process, the charge transfer resistance (R_{ct}) decreases rapidly as the voltage increases from 1.35 to 1.40 V *vs.* RHE, indicating the commencement of the CHA reaction. At a potential of 1.45 V *vs.* RHE, the interfacial reaction impedance of V_O-NiCo$(OH)_2$ is significantly lower than that of catalyst NiCo$(OH)_2$, with R_{ct} values of only 46.8 Ω for V_O-NiCo$(OH)_2$ and 249 Ω for NiCo$(OH)_2$. This indicates that the introduction of V_O induces faster charge transfer and reaction kinetics on the catalyst interface. When the potential increases to 1.50 V *vs.* RHE, the competitive OER reaction leads to a slight increase in interfacial resistance.

Mechanistic study by *in situ* XAS, Raman and IR spectroscopy

To elucidate the dynamic changes in the electronic configuration and atomic surroundings of the Ni and Co active sites within V_O-NiCo$(OH)_2$ during COR, *in situ* X-ray absorption spectroscopy (XAS) analyses were conducted. As illustrated in Fig. 4a, the Ni K-edge XANES spectra reveal variations in the absorption edge position of Ni at different potentials. Initially, the spectrum for Ni at 1.20 V *vs.* RHE aligns with that at the open-circuit potential (OCP), suggesting minimal alterations in Ni electronic structure. As the voltage is incrementally raised from 1.30 V to 1.50 V *vs.* RHE, a positive shift in the near-edge absorption of Ni is observed, indicating an increase in the average oxidation state of Ni throughout the OER. The notable valence change between 1.30 and 1.40 V *vs.* RHE indicates that at 1.40 V *vs.* RHE, high-valent nickel species are produced more rapidly.[25,51,59] Conversely, the valence state of Ni undergoes a negative shift at 1.60 V *vs.* RHE, likely due to the occurrence of the oxygen evolution reaction, which depletes some high-valent Ni species, resulting in a lower valence state. In contrast to the OER, the valence state of Ni increases gradually during COR at 1.40 V *vs.* RHE (Fig. 4b), indicating that the presence of CHA inhibits the formation of high-valent Ni species. This observation correlates with *in situ* impedance measurements, whereby CHA reacts at 1.40 V *vs.* RHE. The Co K-edge XAS spectra shown in Fig. 4c-d indicate that Co undergoes a valence transition starting at a lower potential of 1.20 V *vs.* RHE during the OER, with a significant increase at 1.30 V *vs.* RHE. This behavior is linked to more favorable transitions from Co^{2+} to Co^{3+} and Co^{3+} to Co^{4+}, in contrast to those observed with Ni. Furthermore, CHA inhibits the valence increase of Co, resulting in a notably lower valence state at 1.30 V *vs.* RHE during the COR. Thus, it can be inferred that the electrooxidation of CHA first produces high-valent metal species, which facilitate the oxidation of CHA, eventually returning to the original low-valent state, as illustrated in Fig. 4e.

The coordination environment of the metal centers in the catalyst was further scrutinized through *in situ* EXAFS analysis. Fig. 4f–i illustrates the changes in metal-oxygen bonds and metal–metal bonds of the Ni K-edge during the OER and COR process. As shown in Fig. 4f, measurements taken at OCP reveal peaks at 1.65 Å and 2.71 Å, which are associated with Ni–O and Ni–M (M = Ni and Co) bonds. As the potential increases to 1.30 V *vs.* RHE, Ni–O and Ni–M move to 1.48 Å and 2.45 Å, implying the conversion of Ni^{2+}–OH into Ni^{3+}–OOH. The analogous transition can be observed during COR, with the exception of a propensity for Ni–O and Ni–M bonds to augment at 1.50 V *vs.* RHE, which validates the redox reactions between CHA and NiOOH (Fig. 4g). No noticeable alteration is seen in Co–O bond length during OER and COR, while a significant reduction is observed in Co–M bond at 1.30 V *vs.* RHE, possibly due to the impact of the absorbed Ni change (Fig. 4h and i). This result suggests that in the V_O-NiCo$(OH)_2$ mediated transformation of CHA, Co serves solely as a catalyst for Ni, rather

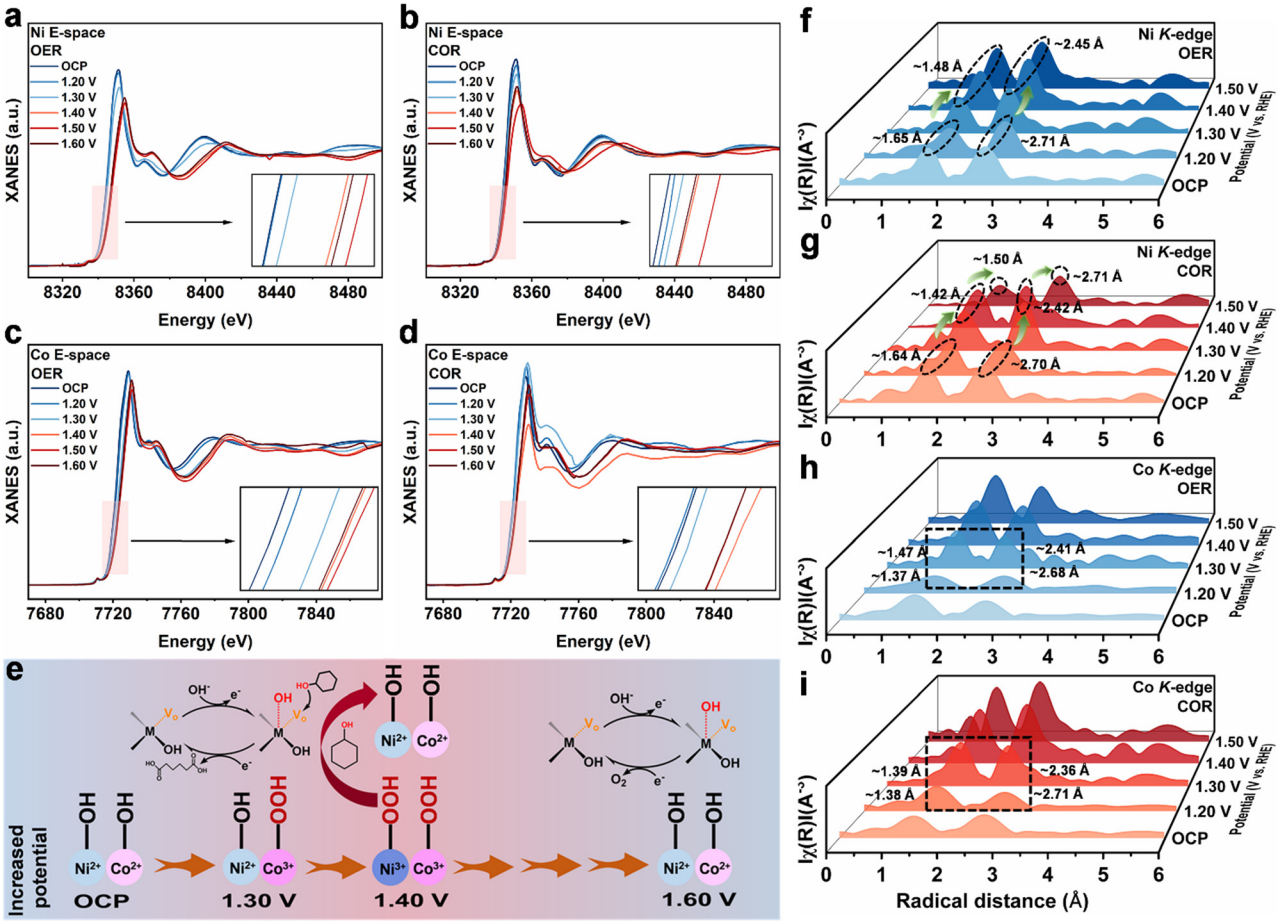

Fig. 4 *In situ* XANES spectra at the Ni K-edge for (a) the OER and (b) COR. *In situ* XANES spectra at the Co K-edge for (c) the OER and (d) COR. (e) Schematic representation of the V_O-NiCo reaction during the OER and COR. *In situ* EXAF spectra for the Ni K-edge during (f) the OER and (g) COR and for the Co K-edge during (h) the OER and (i) COR.

than participating directly in the oxidation process of CHA (Fig. S18, ESI†). The fitted data for Ni and Co K-edge are summarized in Fig. S19–S23 and Tables S3, S4 (ESI†), in which the coordination numbers of Ni and Co in COR are higher than those in the OER, indicating that the presence of oxygen vacancies provides adsorption sites for CHA and intermediates, which enhances the efficiency of the electrosynthesis of AA.

In situ Raman spectroscopy was utilized to elucidate the active catalytic species and the role of oxygen vacancies during the OER and COR processes. For V_O-NiCo(OH)$_2$ at OCP, characteristic peaks around 461 and 527 cm^{-1} were observed (Fig. 5a and b), attributed to Ni^{2+}/Co^{2+}–OH and Ni^{2+}/Co^{2+}–O.[50,54] During the OER process, new peaks emerged at 470 and 550 cm^{-1} when the potential was increased to 1.32 V *vs.* RHE, corresponding to E_g bending and A_g stretching vibrations of Ni^{3+}–O in β-NiOOH.[48,53,60,61] In the presence of CHA, the typical β-NiOOH peaks were delayed until 1.36 V *vs.* RHE, indicating that Ni^{3+}–OOH formed at lower potentials could be reduced to Ni^{2+}–OH by CHA. The intensity of β-NiOOH at 470 and 550 cm^{-1} in COR decreased progressively with increasing potential compared to OER, demonstrating that β-NiOOH was the primary active species.[28,42,58,62,63] Additionally, it can be seen that CHA exhibits reactivity at a low potential of 1.32 V, which aligns with the electrochemical linear sweep voltammetry (LSV) data. Fig. 5c shows the *in situ* Raman spectra of NiCo(OH)$_2$ during COR. When the potential was increased to 1.40 V *vs.* RHE, the characteristic peak of β-NiOOH was detected on the catalyst surface, indicating the conversion of Ni^{2+} into Ni^{3+}. Contrary to V_O-NiCo(OH)$_2$, the β-NiOOH peak for NiCo(OH)$_2$ was not significant at 1.36 V *vs.* RHE, indicating that NiCo(OH)$_2$ is less efficient in generating active species compared to V_O-NiCo(OH)$_2$. Additionally, there was no reduction in the intensity of β-NiOOH in NiCo(OH)$_2$ from 1.40 V to 1.52 V *vs.* RHE. This finding suggests that the incorporation of oxygen vacancies not only enhances the production of active species but also modulates the competitive adsorption of CHA_{ads} and OH_{ads} on the catalyst surface, thereby facilitating the CHA conversion (Fig. 5d). Concurrently, the adsorption and reaction process of CHA was initially characterized by *in situ* Raman spectroscopy. As depicted in Fig. 5c and S24, the peaks at 791, 1030, 1260, 1446, 2862, and 2948 cm^{-1} at OCP correspond to the characteristic peaks of CHA. When the potential was increased from 1.36 to 1.42 V *vs.* RHE, these peaks almost completely vanished, and new peaks appeared at 934,

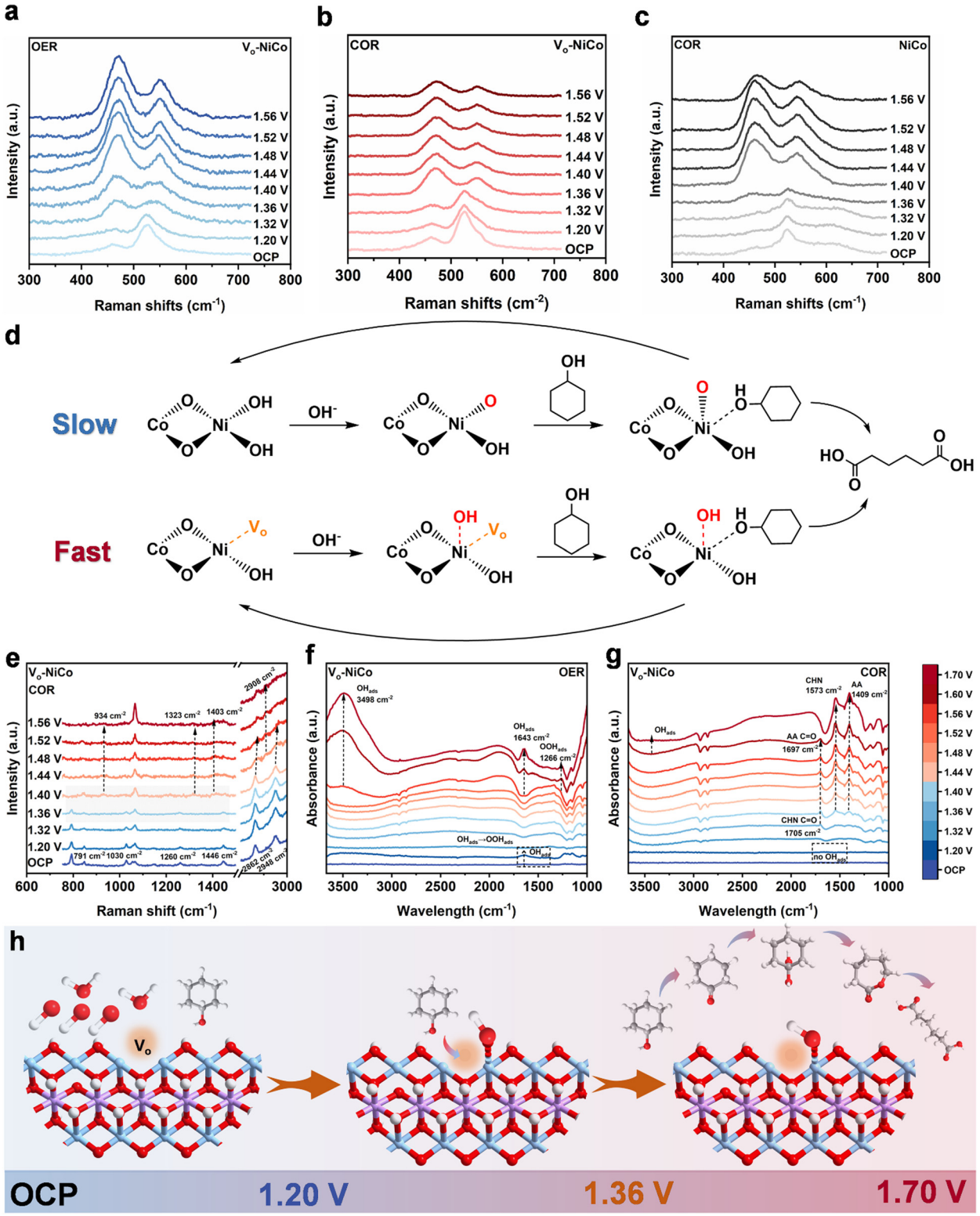

Fig. 5 *In situ* Raman spectra of V_O-NiCo(OH)$_2$ at different potentials during the (a) OER and (b) COR. (c) *In situ* Raman spectra of NiCo(OH)$_2$ at different potentials during the OER. (d) Oxygen vacancies promote active species generation and accelerate the COR. (e) *In situ* Raman monitoring of CHA conversion over V_O-NiCo(OH)$_2$. *In situ* IR spectra of V_O-NiCo(OH)$_2$ at different potentials during the (f) OER and (g) COR. (h) Schematic of the accelerated COR process on the V_O-NiCo(OH)$_2$ surface.

1323, 1403, and 2908 cm^{-1}, indicating the transformation from CHA to CHN and AA.

We further explored the use of *in situ* infrared spectroscopy to observe surface transformations during the COR process directly.

To elucidate the role of oxygen vacancies in the modulation of CHA and OH^-, we initially examined the OER process independently. As depicted in Fig. 5f, notable OH_{ads} stretching and bending vibration peaks emerged at 1643 and 3498 cm^{-1} upon applying a potential of 1.20 V *vs.* RHE, attributable to the accumulation of H_2O and OH^-. When the potential was elevated from 1.32 to 1.52 V *vs.* RHE, a negative absorption of the OH_{ads} vibrational peaks was clearly observed. This phenomenon indicates that the surface-enriched OH^- was involved in the catalytic transformation under potential modulation, leading to the formation of Ni/Co–OOH active species. Conversely, for $NiCo(OH)_2$ shown in Fig. S25 (ESI†), no negative OH_{ads} absorption was observed at low potentials, implying that the OH_{ads} conversion was less efficient and not conducive to the generation of active species Ni/Co–OOH. The OER commenced at potentials exceeding 1.56 V *vs.* RHE, and the OER intermediate was identified at 1266 cm^{-1}. During the COR process (Fig. 5g and h), initially, the OH_{ads} vibrational peak was undetected at 1.20 V *vs.* RHE, indicating a substantial presence of CHA and OH^- on the catalyst surface in equilibrium. Upon increasing the potential to 1.36 V *vs.* RHE, a distinct –C═O stretching vibrational peak appeared at 1705 cm^{-1}, marking the onset of the CHA reaction at that potential. With further potential increase, the peak shifted negatively to 1697 cm^{-1}, indicating the continued oxidation of CHA leading to the formation of AA. Similar alterations were observed at 1573 and 1409 cm^{-1}.

Conclusions

A V_O-$NiCo(OH)_2$ electrocatalyst was developed for the proficient electrosynthesis of AA from CHA. Computational analysis indicates that oxygen vacancies modulate the electronic configuration of the metal active sites, thereby optimizing CHA activation and OH^- adsorption on the catalyst surface. This adjustment enhances the OH^- mediated attack on the C_α position, facilitating the formation of the pivotal intermediate 1,1-dihydroxycyclohexane, and subsequently promoting the highly selective production of AA. Electrochemical evaluations demonstrated that V_O-$NiCo(OH)_2$ exhibited exceptional catalytic performance with conversion efficiency, AA selectivity, and faradaic efficiency rates of 98.4%, 95.6%, and 95.2%, respectively, and generated hydrogen at a rate 8.2 times higher than that achieved by pure water electrolysis at the cathode. *In situ* Raman and infrared spectroscopy corroborated that oxygen vacancies aid in the formation of the active species NiOOH, enhance CHA adsorption and activation on the catalyst surface, and expedite electron transfer processes between CHA and NiOOH. This methodology introduces an innovative strategy for producing clean energy materials from renewable feedstocks using cost-effective catalysts, addressing the pressing issues of energy resource depletion and environmental pollution, thus contributing to sustainable energy development.

Author contributions

G. H. Z. conceived the idea and led the project. X. P. designed and performed the majority of the experiments. L. Z. S. recorded the HAADF-STEM images and analyzed the data. X. P. and L. Z. S. carried out XAS characterizations. X. P., J. G. Z. and S. X. performed the electrochemical data analysis. X. P. and C. M. carried out XAFS characterizations. X. P. and K. C. processed the theoretical calculation data. X. P. and G. H. Z. wrote the paper. All the authors have discussed the results.

Conflicts of interest

There are no conflicts to declare.

Data availability

The data supporting this article have been included as part of the ESI.†

Acknowledgements

This work was financially supported by the National Natural Science Foundation of China (NSFC, grant No. 22476153, 22076140, and 21537003), the National Key R&D Program of China (grant no. 2024YFA1211003) and the Tongji University Medicine-X Interdisciplinary Research Initiative (grant No. 2025-0313-ZD-02). Additionally, we thank the Shanghai Synchrotron Radiation Facility of BL11B and BL16U1 (SSRF, No. 2022-SSRF-PT-501407, 2024-SSRF-PT-506945, and 2024-SSRF-PT-506949) for the assistance with XAFS measurements.

References

1 J. Li and H. Duan, *Chem*, 2024, **10**, 3008–3039.
2 Y. Li, X. Wei, L. Chen and J. Shi, *Angew. Chem., Int. Ed.*, 2021, **60**, 19550–19571.
3 H. Luo, J. Barrio, N. Sunny, A. Li, L. Steier, N. Shah, I. E. L. Stephens and M.-M. Titirici, *Adv. Energy Mater.*, 2021, **11**, 2101180.
4 J.-T. Ren, L. Chen, H.-Y. Wang, W.-W. Tian and Z.-Y. Yuan, *Energy Environ. Sci.*, 2024, **17**, 49–113.
5 H. Sun, X. Xu, L. Fei, W. Zhou and Z. Shao, *Adv. Energy Mater.*, 2024, **14**, 2401242.
6 P. Wang, J. Zheng, X. Xu, Y.-Q. Zhang, Q.-F. Shi, Y. Wan, S. Ramakrishna, J. Zhang, L. Zhu, T. Yokoshima, Y. Yamauchi and Y.-Z. Long, *Adv. Mater.*, 2024, **36**, 2404806.
7 K. Zhang, Q. Meng, H. Wu, J. Yan, X. Mei, P. An, L. Zheng, J. Zhang, M. He and B. Han, *J. Am. Chem. Soc.*, 2022, **144**, 20834–20846.
8 J. Barluenga, F. González-Bobes, S. R. Ananthoju, M. A. García-Martín and J. M. González, *Angew. Chem., Int. Ed.*, 2001, **40**, 3389–3392.
9 H. Hattori, Y. Ide, S. Ogo, K. Inumaru, M. Sadakane and T. Sano, *ACS Catal.*, 2012, **2**, 1910–1915.
10 J. Yang, J. Liu, H. Neumann, R. Franke, R. Jackstell and M. Beller, *Science*, 2019, **366**, 1514–1517.
11 T. Schaub, *Science*, 2019, **366**, 1447.

12 W. Deng, L. Yan, B. Wang, Q. Zhang, H. Song, S. Wang, Q. Zhang and Y. Wang, *Angew. Chem., Int. Ed.*, 2021, **60**, 4712–4719.
13 J. Rios, J. Lebeau, T. Yang, S. Li and M. D. Lynch, *Green Chem.*, 2021, **23**, 3172–3190.
14 S. Van de Vyver and Y. Román-Leshkov, *Catal. Sci. Technol.*, 2013, **3**, 1465–1479.
15 K. C. Hwang and A. Sagadevan, *Science*, 2014, **346**, 1495–1498.
16 Z. Li, X. Li, H. Zhou, Y. Xu, S.-M. Xu, Y. Ren, Y. Yan, J. Yang, K. Ji, L. Li, M. Xu, M. Shao, X. Kong, X. Sun and H. Duan, *Nat. Commun.*, 2022, **13**, 5009.
17 F. Liu, X. Gao, Z. Guo, E. C. M. Tse and Y. Chen, *J. Am. Chem. Soc.*, 2024, **146**, 15275–15285.
18 F. Liu, X. Gao, R. Shi, J. Xiong, Z. Guo, E. C. M. Tse and Y. Chen, *Adv. Funct. Mater.*, 2024, **34**, 2310274.
19 M. Qin, R. Fan, J. Chen, H. Wang, X. Zheng, S. Mao, R. Du and Y. Wang, *Chem. Eng. J.*, 2022, **442**, 136264.
20 W. Chen, C. Xie, Y. Wang, Y. Zou, C.-L. Dong, Y.-C. Huang, Z. Xiao, Z. Wei, S. Du, C. Chen, B. Zhou, J. Ma and S. Wang, *Chem*, 2020, **6**, 2974–2993.
21 X. Luo, B. Wu, J. Li, Y. Wang, X. Tang, C. Li, M. Shao and Z. Wei, *J. Am. Chem. Soc.*, 2023, **145**, 20665–20671.
22 B. Jin, J. Gao, Y. Zhang and M. Shao, *Smart Mol.*, 2024, **2**, e20230026.
23 Y. Lu, H. Wang, Q. Li, Q. Liu, X. Zhang, Y. Jia, X. Cai, Z. Zhao, Y. Huan and B. Z. Tang, *Smart Mol.*, 2025, **3**, e20240011.
24 Y. Jia, Z. Chen, B. Gao, Z. Liu, T. Yan, Z. Gui, X. Liao, W. Zhang, Q. Gao, Y. Zhang, X. Xu and Y. Tang, *J. Am. Chem. Soc.*, 2024, **146**, 1282–1293.
25 X. Liu, Y.-Q. Zhu, J. Li, Y. Wang, Q. Shi, A.-Z. Li, K. Ji, X. Wang, X. Zhao, J. Zheng and H. Duan, *Nat. Commun.*, 2024, **15**, 7685.
26 X. Liu, X. Wang, C. Mao, J. Qiu, R. Wang, Y. Liu, Y. Chen and D. Wang, *Angew. Chem., Int. Ed.*, 2024, **63**, e202408109.
27 G. Liu, T. Nie, Z. Song, X. Sun, T. Shen, S. Bai, L. Zheng and Y.-F. Song, *Angew. Chem., Int. Ed.*, 2023, **62**, e202311696.
28 D. Chen, Y. Ding, X. Cao, L. Wang, H. Lee, G. Lin, W. Li, G. Ding and L. Sun, *Angew. Chem., Int. Ed.*, 2023, **62**, e202309478.
29 Y. Xie, Z. Zhou, N. Yang and G. Zhao, *Adv. Funct. Mater.*, 2021, **31**, 2102886.
30 Z. Yang, L. Chen, Y. Yin, C. Wei, Z. Xue and T. Mu, *Energy Environ. Sci.*, 2024, **17**, 8801–8809.
31 D. Chen, W. Li, J. Liu and L. Sun, *Energy Environ. Sci.*, 2025, **18**, 3120–3128.
32 Y. Yan, J. Zhong, R. Wang, S. Yan and Z. Zou, *J. Am. Chem. Soc.*, 2024, **146**, 4814–4821.
33 L. Xu, Z. Huang, M. Yang, J. Wu, W. Chen, Y. Wu, Y. Pan, Y. Lu, Y. Zou and S. Wang, *Angew. Chem., Int. Ed.*, 2022, **61**, e202210123.
34 J. Zheng, X. Chen, X. Zhong, S. Li, T. Liu, G. Zhuang, X. Li, S. Deng, D. Mei and J.-G. Wang, *Adv. Funct. Mater.*, 2017, **27**, 1704169.
35 W. Wang, Y. Wang, R. Yang, Q. Wen, Y. Liu, Z. Jiang, H. Li and T. Zhai, *Angew. Chem., Int. Ed.*, 2020, **59**, 16974–16981.
36 L. Sun, Z. Zhou, Y. Xie, J. Zheng, X. Pan, L. Li and G. Zhao, *Adv. Funct. Mater.*, 2023, **33**, 2301884.
37 L. Chen, Z.-H. Yin, J.-Y. Cui, C.-Q. Li, K. Song, H. Liu and J.-J. Wang, *J. Am. Chem. Soc.*, 2024, **146**, 27090–27099.
38 C. Huang, Y. Huang, C. Liu, Y. Yu and B. Zhang, *Angew. Chem., Int. Ed.*, 2019, **58**, 12014–12017.
39 Z. Zhou, X. Pan, L. Sun, Y. Xie, J. Zheng, L. Li and G. Zhao, *Angew. Chem., Int. Ed.*, 2023, **62**, e202216347.
40 R. Wang, Y. Kang, J. Wu, T. Jiang, Y. Wang, L. Gu, Y. Li, X. Yang, Z. Liu and M. Gong, *Angew. Chem., Int. Ed.*, 2022, **61**, e202214977.
41 M. Zubair, P. M. Usov, H. Ohtsu, J. A. Yuwono, C. S. Gerke, G. D. Y. Foley, H. Hackbarth, R. F. Webster, Y. Yang, W. H. Lie, Z. Ma, L. Thomsen, M. Kawano and N. M. Bedford, *Adv. Energy Mater.*, 2024, **14**, 2400676.
42 Y. Sun, J. Wang, Y. Qi, W. Li and C. Wang, *Adv. Sci.*, 2022, **9**, 2200957.
43 X. Deng, G.-Y. Xu, Y.-J. Zhang, L. Wang, J. Zhang, J.-F. Li, X.-Z. Fu and J.-L. Luo, *Angew. Chem., Int. Ed.*, 2021, **60**, 20535–20542.
44 Y. Lu, T. Liu, C.-L. Dong, C. Yang, L. Zhou, Y.-C. Huang, Y. Li, B. Zhou, Y. Zou and S. Wang, *Adv. Mater.*, 2022, **34**, 2107185.
45 Y. Yang, W. H. Lie, R. R. Unocic, J. A. Yuwono, M. Klingenhof, T. Merzdorf, P. W. Buchheister, M. Kroschel, A. Walker, L. C. Gallington, L. Thomsen, P. V. Kumar, P. Strasser, J. A. Scott and N. M. Bedford, *Adv. Mater.*, 2023, **35**, 2305573.
46 Z. Xia, C. Ma, Y. Fan, Y. Lu, Y.-C. Huang, Y. Pan, Y. Wu, Q. Luo, Y. He, C.-L. Dong, S. Wang and Y. Zou, *ACS Catal.*, 2024, **14**, 1930–1938.
47 W. Chen, J. Shi, Y. Wu, Y. Jiang, Y.-C. Huang, W. Zhou, J. Liu, C.-L. Dong, Y. Zou and S. Wang, *Angew. Chem., Int. Ed.*, 2024, **63**, e202316449.
48 D. Xiao, X. Bao, D. Dai, Y. Gao, S. Si, Z. Wang, Y. Liu, P. Wang, Z. Zheng, H. Cheng, Y. Dai and B. Huang, *Adv. Mater.*, 2023, **35**, 2304133.
49 Q. Qian, J. Zhang, J. Li, Y. Li, X. Jin, Y. Zhu, Y. Liu, Z. Li, A. El-Harairy, C. Xiao, G. Zhang and Y. Xie, *Angew. Chem., Int. Ed.*, 2021, **60**, 5984–5993.
50 B. Zhu, B. Dong, F. Wang, Q. Yang, Y. He, C. Zhang, P. Jin and L. Feng, *Nat. Commun.*, 2023, **14**, 1686.
51 L. Sun, X. Pan, Y.-N. Xie, J. Zheng, S. Xu, L. Li and G. Zhao, *Angew. Chem., Int. Ed.*, 2024, **63**, e202402176.
52 J. Zhang, Y. Shen, Z. Wu, X. Zhang, J. Kang, Y. Wu, S. Zhang, S. Chen, G. Wang, H. Zhang, H. Yin and H. Zhao, *Angew. Chem., Int. Ed.*, 2025, **64**, e202423109.
53 Z. He, J. Hwang, Z. Gong, M. Zhou, N. Zhang, X. Kang, J. W. Han and Y. Chen, *Nat. Commun.*, 2022, **13**, 3777.
54 Z. Li, S. Ning, J. Xu, J. Zhu, Z. Yuan, Y. Wu, J. Chen, F. Xie, Y. Jin, N. Wang, H. Meng and S. Sun, *Energy Environ. Sci.*, 2022, **15**, 5300–5312.
55 T. Wu, X. Zhu, G. Wang, Y. Zhang, H. Zhang and H. Zhao, *Nano Res.*, 2018, **11**, 1004–1017.
56 K. Ji, Y. Liu, Y. Wang, K. Kong, J. Li, X. Liu and H. Duan, *J. Am. Chem. Soc.*, 2024, **146**, 11876–11886.
57 S. Guo, C. Wang, H. Li, T. Li, C. Liu, Y. Gao, B.-H. Zhao and B. Zhang, *Angew. Chem., Int. Ed.*, 2025, **64**, e202423432.

58 Z. Yang, S. Wang, C. Wei, L. Chen, Z. Xue and T. Mu, *Energy Environ. Sci.*, 2024, **17**, 1603–1611.
59 W. Cheng, S. Xi, Z.-P. Wu, D. Luan and X. W. Lou, *Sci. Adv.*, 2021, **7**, eabk0919.
60 H. Qin, Y. Ye, J. Li, W. Jia, S. Zheng, X. Cao, G. Lin and L. Jiao, *Adv. Funct. Mater.*, 2023, **33**, 2209698.
61 H. Huang, C. Yu, X. Han, H. Huang, Q. Wei, W. Guo, Z. Wang and J. Qiu, *Energy Environ. Sci.*, 2020, **13**, 4990–4999.
62 L. Zheng, Y. Zhao, P. Xu, Z. Lv, X. Shi and H. Zheng, *J. Mater. Chem. A*, 2022, **10**, 10181–10191.
63 Z. Zhou, Y.-n Xie, L. Sun, Z. Wang, W. Wang, L. Jiang, X. Tao, L. Li, X.-H. Li and G. Zhao, *Appl. Catal., B*, 2022, **305**, 121072.